Impurity Retention Effect in the Edge Ergodic Layer of the Large Helical Device

Masahiro KOBAYASHI, Yuehe FENG[1)], Sigeru MORITA, Kuninori SATO,
Malay Bikas CHOWDHURI[2)], Suguru MASUZAKI, Mamoru SHOJI, Yukio NAKAMURA,
Masayuki TOKITANI, Nobuyoshi OHYABU, Motoshi GOTO, Tomohiro MORISAKI,
Ichihiro YAMADA, Kazumichi NARIHARA, Naoko ASHIKAWA, Hiroshi YAMADA,
Akio KOMORI, Osamu MOTOJIMA and the LHD experimental group

National Institute for Fusion Science, Toki 509-5292, Japan
[1)]*Max-Planck-Institute fuer Plasmaphysik, Wendelsteinstrasse 1, D-17491 Greifswald, Germany*
[2)]*Graduate University for Advanced Studies, Toki, Gifu 509-5292, Japan*

(Received 30 November 2007 / Accepted 12 March 2008)

The impurity transport characteristics in the ergodic layer of the Large Helical Device (LHD) are analyzed using the 3D edge transport code (EMC3-EIRENE), in comparison with the experimental data. The 3D modeling predicts the impurity retention (screening) in the ergodic layer at the high-density plasma. It is found that the edge surface layer plays an important role in impurity retention, where the friction force significantly dominates over the thermal force. The line intensity measurements of CIII to CVI show consistent behavior with the modeling, indicating impurity retention in the ergodic layer. The applicability of the model for high-*Z* impurity is also discussed, and it is found that the experimental data is consistent with the results of edge transport modeling.

Keywords: ergodic layer, impurity transport, LHD

DOI: 10.1585/pfr.3.S1005

1. Introduction

Control of impurity transport in a fusion device is one of the most important issues, to avoid impurity contamination of core plasma, which leads to confinement degradation by radiative cooling, as well as reduction of fusion power due to fuel dilution [1]. The impurity that is released at divertor plates or the first wall reaches the scrape-off layer (SOL), where they experience ionization and are thereby transported as charged particles. The transport in the SOL then determines the influx of the impurity to the core region [2]. This paper focuses on the impurity transport in the edge region, especially the effect of the stochastic magnetic field. It has been reported in Tore Supra experiments that there is an indication of plasma decontamination in the ergodic divertor configuration [3], and this phenomena was discussed using an (1D) analytical model [4, 5], as an enhanced outflux of plasma by the stochastic field lines, which tends to exhaust the impurity. A similar explanation was also provided by D. Kh. Morozov *et al.* [6].

On the other hand, the Large Helical Device (LHD) in the National Institute for Fusion Science intrinsically has the ergodic layer in the edge region. It is found that even with an extremely high core density operation, where the negative radial electric field is formed, it is free from radiation collapse, suggesting no serious impurity contamination [7]. In this paper, we discuss impurity transport in the edge ergodic region of the LHD using a 3D numerical transport code that considers all relevant terms of the impurity transport model and the precise magnetic field configuration (i.e. braiding magnetic field). This enables us to directly compare the impurity transport model with experimental results, which gives us a clearer interpretation of the impurity transport process in the ergodic layer.

2. Magnetic Field Structure of Ergodic Layer in LHD

The LHD is a heliotron-type device with steady state magnetic field sustained by superconducting helical coils of $l = 2$. The major and averaged minor radii are 3.9 and ~1.0 m, respectively [8]. The helical coils' winding creates a magnetic field structure of 10 field periods in the toroidal direction. The radial magnetic field caused by the helical coils with many different modes produces magnetic islands at the edge region, and they overlap to create an ergodic field structure there.

The connection length profile of the ergodic layer is plotted in Fig. 1, along with the Poincare map. r_{eff} is indicated in the vertical axis at the right side, which is defined by the cylindrical approximation of the volume enclosed by the radial surface of the computational mesh. In Fig. 1, the radial and poloidal mesh surfaces are aligned horizon-

---

author's e-mail: kobayashi.masahiro@lhd.nifs.ac.jp

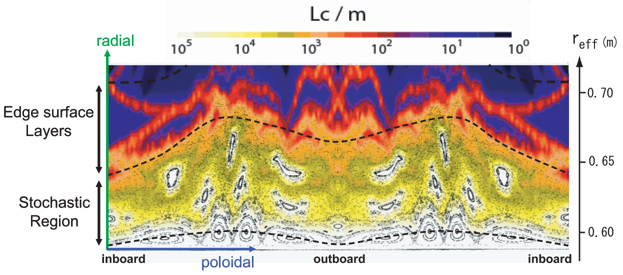

Fig. 1 Connection length (L_C) profile in ergodic layer of LHD, superposed with Poincare plot of field lines. L_C is resolved up to 100 km. r_{eff} is indicated in the vertical axis at the right side, which is defined by cylindrical approximation of the volume enclosed by the radial surface of computational mesh.

tally and vertically, respectively. In this study, the ergodic layer is divided into three regions, following the terminology of Ref. [8], which is defined based on the magnetic field topology that affects the transport properties of plasma (impurity), as shown later. The region with $m = 8$ magnetic islands is considered as the confinement region because of the clear island structure and the long connection length (> 100 km). The stochastic region starts from $m = 7$ islands, where they are overlapping with the neighboring islands and the separatrix is no longer clear. The region starting from the mode of $m = 4$, is called the edge surface layer, where short and long field lines are mixed. This structure is a unique feature of the heliotron divertor configuration, which is created by strong magnetic shear that stretches and bends the flux tubes, and thus mixes up the long and short flux tubes. The outside of the edge surface layer has divertor legs, which connect to the divertor plate, which is not shown in Fig. 1.

3. Impurity Transport Analysis in the Ergodic Layer

The impurity transport analysis has been performed using the edge transport code EMC3 [9] - EIRENE [10], for considering the magnetic field structure of the ergodic layer. The code solves the fluid equations of the mass, momentum, and energy in the steady state based on the Braginskii's formulation,

$$\nabla \cdot (n_i V_{i\parallel} \boldsymbol{b} - D \boldsymbol{b}_\perp \boldsymbol{b}_\perp \cdot \nabla n_i) = S_p, \tag{1}$$

$$\begin{aligned}\nabla \cdot (m_i n_i V_{i\parallel} V_{i\parallel} \boldsymbol{b} - \eta_\parallel \boldsymbol{bb} \cdot \nabla V_{i\parallel} - m_i V_{i\parallel} D \boldsymbol{bb} \cdot \nabla n_i \\ - \eta_\perp \boldsymbol{b}_\perp \boldsymbol{b}_\perp \cdot \nabla V_{i\parallel}) = -\boldsymbol{b} \cdot \nabla (n_e T_e + n_i T_i) + S_m,\end{aligned} \tag{2}$$

$$\begin{aligned}\nabla \cdot \Bigg(\frac{5}{2} n_e T_e V_{i\parallel} \boldsymbol{b} - \kappa_e \boldsymbol{bb} \cdot \nabla T_e - \frac{5}{2} T_e D \boldsymbol{b}_\perp \boldsymbol{b}_\perp \cdot \nabla n_e \\ - \chi_e n_e \boldsymbol{b}_\perp \boldsymbol{b}_\perp \cdot \nabla T_e \Bigg) = -k(T_e - T_i) + S_{ee} + S_{imp},\end{aligned} \tag{3}$$

$$\begin{aligned}\nabla \cdot \Bigg(\frac{5}{2} n_i T_i V_{i\parallel} \boldsymbol{b} - \kappa_i \boldsymbol{bb} \cdot \nabla T_i - \frac{5}{2} T_i D \boldsymbol{b}_\perp \boldsymbol{b}_\perp \cdot \nabla n_i \\ - \chi_i n_i \boldsymbol{b}_\perp \boldsymbol{b}_\perp \cdot \nabla T_i \Bigg) = k(T_e - T_i) + S_{ei},\end{aligned} \tag{4}$$

where $\boldsymbol{b}$ is the unit vector of the magnetic field and $\boldsymbol{b}_\perp \boldsymbol{b}_\perp = \mathsf{I} - \boldsymbol{bb}$, with I being a unit tensor. n_i, $V_{i\parallel}$, T_e, and T_i are the ion density, parallel ion velocity, electron temperature, and ion temperature of the background plasma, respectively. S_p and S_m are the particle and the momentum, respectively, and S_{ee} and S_{ei} are the energy sources associated with neutrals. S_{imp} represents the energy loss due to impurity radiations. $\eta_\parallel$ and $\kappa_{e,i}$ are the parallel viscosity and heat conductivity of an electron/ion, respectively, for which classical formulations are used. D, $\eta_\perp (= m_i n_i D)$ and $\chi_{e,i}$ are the perpendicular particle diffusivity, viscosity, and heat diffusivity, respectively. These are assumed to be anomalous. For impurity, the continuity and momentum balance equations for the charged state Z are given by

$$\begin{aligned}\nabla \cdot (n_z V_{z\parallel} \boldsymbol{b} - D_z \boldsymbol{b}_\perp \boldsymbol{b}_\perp \cdot \nabla n_z) = S_{z-1\to z} n_{z-1} \\ - S_{z\to z+1} n_z + R_{z+1\to z} n_{z+1} - R_{z\to z-1} n_z,\end{aligned} \tag{5}$$

$$\begin{aligned}0 = -\frac{1}{n_z} \boldsymbol{b} \cdot \nabla n_z T_z + m_z \frac{V_{z\parallel} - V_{i\parallel}}{\tau_s} \\ + ZeE_\parallel + C_e \boldsymbol{b} \cdot \nabla T_e + C_i \boldsymbol{b} \cdot \nabla T_i,\end{aligned} \tag{6}$$

where it is assumed that $T_z = T_i$, and τ_s and $E_\parallel$ are the impurity-ion collision time and parallel electric field, respectively. $C_i \approx 2.6Z^2$ and $C_e \approx 0.71Z^2$. $E_\parallel$ is obtained by Ohm's law as follows:

$$\boldsymbol{b} \cdot \nabla n_e T_e + n_e e E_\parallel + n_e C_e \boldsymbol{b} \cdot \nabla T_e = 0. \tag{7}$$

The recycling neutrals are released from the divertor plates being proportional to the particle deposition pattern obtained by EMC3. The neutrals are traced by EIRENE experiencing various atomic processes with plasma until they are ionized. After the ionization which goes into S_p in Eq. (1), the plasma transport starts. The boundary conditions at the inner most surface (LCFS) for particle, momentum, energy transport are reflection, zero velocity and constant energy flux, respectively. The energy flux, which is equally split to electrons and ions, is distributed in the poloidal and toroidal directions considering the magnetic flux surface expansion. The boundary condition at the outer most surface is the sink of the particle, momentum, and energy with a decay length of several cm. The boundary is located to cover the maximum possible area of the plasma such that the loss at the surface through perpendicular transport is less than a few percent of the total amount of the particles and energy, so that the assumed decay length does not affect the results of the computations. At the divertor plate, the Bohm condition is imposed for the particles, momentum, and energy transport, respectively. Therefore, the input parameters for computations are D, $\chi_{e,i}$ and total power flowing to the SOL, P_{SOL}. D, $\chi_{e,i}$ are adjusted to fit experimental data, keeping the relation $\chi = 3D$, and P_{SOL} is estimated from deposition power of the NBI and radiation loss in the core region. For the present analysis, these are set as $D = 0.5$, $\chi_{e,i} = 1.5\ \mathrm{m^2/s}$, and $P_{SOL} = 8\ \mathrm{MW}$.

In Eq. (6), the first term on the right hand side is the pressure gradient force of the impurity. The second term, the friction force, and the third term, the parallel electric field, are usually directed to the divertor, while the forth and fifth terms on the right-hand side, the electron and ion thermal force pull the impurity upstream because of the parallel temperature drop to the divertor plate. It is easily shown that the dominating terms in the equation are the ion thermal force and the friction force [11, 12]. In force balance, Eq. (6), therefore becomes

$$V_{z\parallel} = V_{i\parallel} + C_i \frac{\tau_s}{m_z} \boldsymbol{b} \cdot \nabla T_i. \qquad (8)$$

Since $V_{i\parallel}$ flows towards the divertor plate, while $\partial T_i/\partial s$ directs upstream, when the friction dominates over the thermal force, the impurity flows to the divertor. The ratio of the friction to the thermal force in Eq. (6) is given by [13, 14],

$$\frac{\text{friction force}}{\text{thermal force}} \sim \frac{5/2 n_i T_i V_{i\parallel}}{\kappa_i^0 T_i^{2.5} \nabla_\parallel T_i} \propto \frac{n_i |M|}{T_i \nabla_\parallel T_i}, \qquad (9)$$

where M is the Mach number. The numerator represents convective energy flux, while the denominator represents conductive energy flux.

Eq. (9) shows that as the plasma becomes dense and cold with a substantial flow acceleration, the friction force dominates over the thermal force, resulting in impurity retention at the divertor. In the present analysis, carbon is selected as the impurity species, which is released at the divertor plate with the source rate being proportional to the divertor flux, and traced according to Eq. (6), also in perpendicular to field lines as diffusive process. The parallel impurity flow velocity and the bulk plasma flow obtained by 3D modeling are plotted in Fig. 2 for different density with fixed input power, where the yellow and black colors mean flows in positive and negative toroidal directions, respectively. In this figure, it is can clearly be seen that at $n_{LCFS} = 2 \times 10^{19}\ \mathrm{m^{-3}}$, the impurity flow direction is opposite to the bulk plasma flow, i.e., the thermal force pushes the impurity upstream, whereas at $n_{LCFS} = 4 \times 10^{19}\ \mathrm{m^{-3}}$, the direction of impurity flow is in same phase as the bulk plasma flow due to the friction force. The resulting total

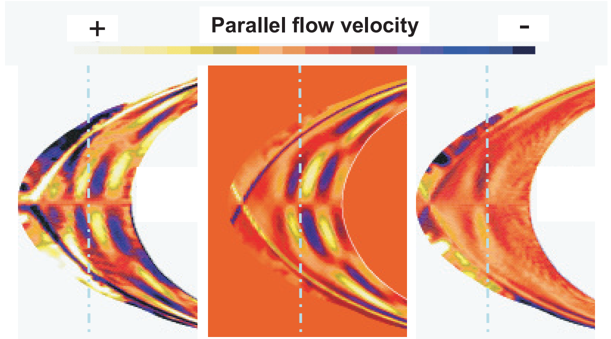

(a) Impurity flow (2e19 m^{-3})

(b) plasma flow

(c) Impurity flow (4e19 m^{-3})

Fig. 2 (a) Parallel impurity flow velocity at $n_{LCFS} = 2 \times 10^{19}\ \mathrm{m^{-3}}$, (b) parallel flow velocity of bulk plasma, (c) same as (a) but for $n_{LCFS} = 4 \times 10^{19}\ \mathrm{m^{-3}}$. The yellow and blue indicate positive and negative flow in toroidal direction. The dashed lines are located at the same radial position for eye guide.

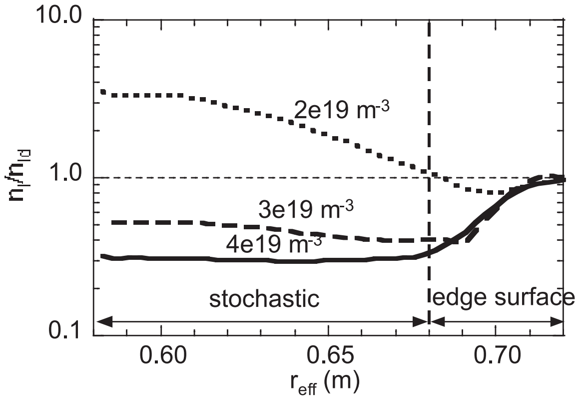

Fig. 3 Radial profiles of carbon density summed up over all charge states, for different density, $n_{LCFS} = 2, 3, 4 \times 10^{19}\ \mathrm{m^{-3}}$ normalized with the downstream density at $r_{eff} = 0.72\ \mathrm{m}$, n_{Id}. r_{eff} is defined by cylindrical approximation of the volume enclosed by the radial surface of computational mesh (Fig. 1). The carbon densities are averaged ones over poloidal and toroidal directions.

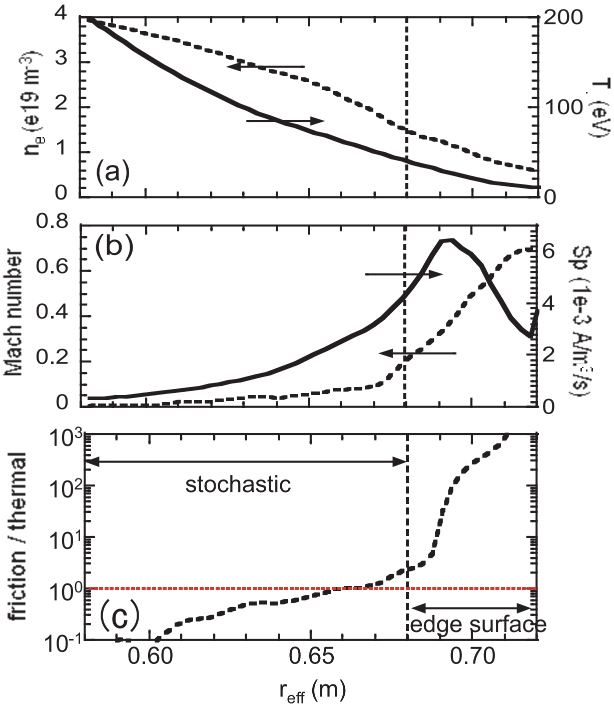

Fig. 4 The radial profiles of (a) n_e and T_i, (b) Mach number and ionization source, and (c) Eq. (9), are averaged in the poloidal and toroidal directions as a function of r_{eff} (Fig. 1) for $n_{LCFS} = 4 \times 10^{19}\ \mathrm{m^{-3}}$.

impurity density (summed up over all charge states) profiles are plotted in Fig. 3, in a radial coordinate $r_{\rm eff}$ for different plasma densities. $r_{\rm eff}$ is defined by cylindrical approximation of the volume enclosed by the radial surface of computational mesh. At a low density, $n_{\rm LCFS} = 2 \times 10^{19}$ m^{-3}, the thermal force is so effective that the impurity is drawn to LCFS, and accumulates there. With increasing density, the upstream impurity density gradually decreases, and at $n_{\rm LCFS} = 4 \times 10^{19}$ m^{-3}, the impurity is driven towards the divertor by the friction force, resulting in divertor retention, as seen in Fig. 3.

As the retention effect is switched on, the profile become flat in the stochastic region and is lower than the downstream where the density gradient is formed, especially in the edge surface layer. The profile indicates that the friction force pushing the impurity outward is effective only in the edge surface layer. Plotted in Fig. 4 (c) is Eq. (9), the ratio of the friction to thermal force, as well as (a) the electron temperature and density, and (b) the Mach number and ionization source of bulk plasma. In the edge surface layer, there appears substantial acceleration of the Mach number, which is considered to be caused by the hydrogen ionization source and also the particle sink due to the short connection length of the flux tubes that are embedded in-between the long ones. The temperature decreases towards the edge. These parameter changes result in a significant increase in the friction-thermal force ratio in the edge surface layer, as seen in Fig. 4 (c).

4. Comparison with Experiments

Figure 5 (a) shows the radial profiles of the carbon density in different charge states at $n_{\rm LCFS} = 4 \times 10^{19}$ m^{-3}, where the impurity retention is effective, as discussed above. For comparison, the profile at $n_{\rm LCFS} = 2 \times 10^{19}$ m^{-3} is plotted in Fig. 5 (b), shows a case in which the impurity accumulates around the LCFS because of the dominant thermal force. Due to the large jump in the ionization potential between C^{+3} (= 64.5 eV) and C^{+4} (= 392 eV), there appears clear separation of the location of the peak positions between the low and high charge states groups, i.e., lower charge states C^{+1}, C^{+2}, and C^{+3} are mainly located at $r_{\rm eff} > 0.67$ m, while the higher ones C^{+4}, C^{+5}, and C^{+6} have peaks at $r_{\rm eff} < 0.67$ m. At $n_{\rm LCFS} = 4 \times 10^{19}$ m^{-3}, it is seen that the lower charge states increases due to the retention effect at the outer radius, and at the same time the density of the higher charge group near the LCFS is suppressed. On the other hand in the case of $n_{\rm LCFS} = 2 \times 10^{19}$ m^{-3}, the higher charge group increases significantly in the inner radius, with reduced lower charge group at the outer radius. The differences in the profiles are reflected in the radiation intensity, which is shown in Fig. 6 (a), where the intensity is integrated for the computational domain of half a field period. The radiation from the lower charge states, CII, CIII, and CIV, increases monotonically by an order of magnitude with increasing bulk plasma density. This is due to both the increase of carbon yield, which is proportional to divertor flux, and the retention effect. On the other hand, the radiation from the higher charge states, CV and CVI, remains almost constant. This is mainly due to the reduction of the density, which is caused by the retention at the higher density, and also partly because of the temperature change caused by density scan, where the CIV and CV are still sensitive to the temperature in the range of 100 to 200 eV. In order to illustrate the impact of friction exerted by bulk plasma flow, $V_{i\parallel}$ is set to zero in Eq. (6), keeping all other parameters unchanged. The results are plotted in Fig. 6. In this case, because of no outward component of impurity flow, the absolute content of the impurity increases, and thus the radiation intensity is relatively higher than in Fig. 6 (a). One should also note the qualitatively different behavior of CV and CVI, i.e., the radiation from the higher charge states (CV and CVI), monotonically increases with increasing density. This is attributed to the large increase of C^{+4} and C^{+5} density at the inner radius of the ergodic layer because of the lack of flushing effect by the bulk plasma flow.

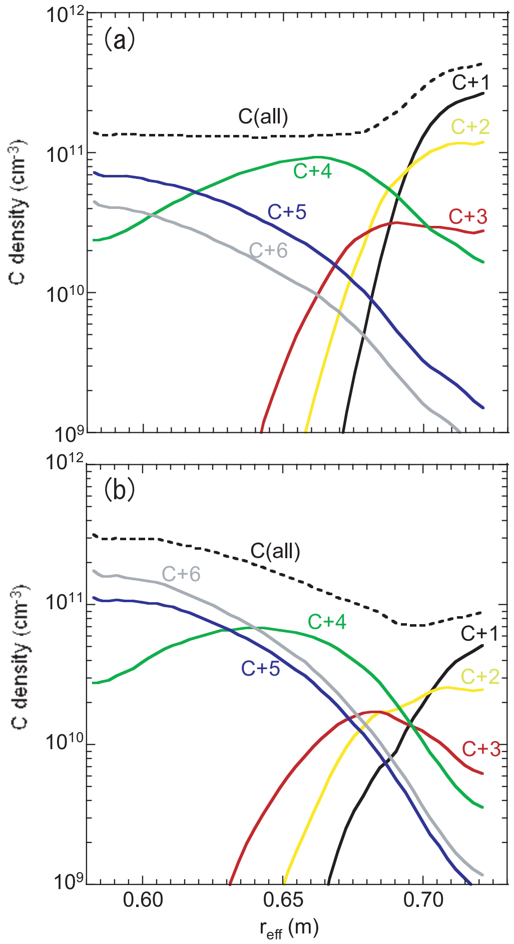

Fig. 5 Radial profiles of carbon density at different charge states, black : C^{+1}, yellow : C^{+2}, red: C^{+3}, green : C^{+4}, blue : C^{+5}, grey : C^{+6}, dashed lines : total density of carbon. (a) $n_{\rm LCFS} = 4 \times 10^{19}$ m^{-3}, (b) $n_{\rm LCFS} = 2 \times 10^{19}$ m^{-3}.

The radiation intensity is measured in the experiments

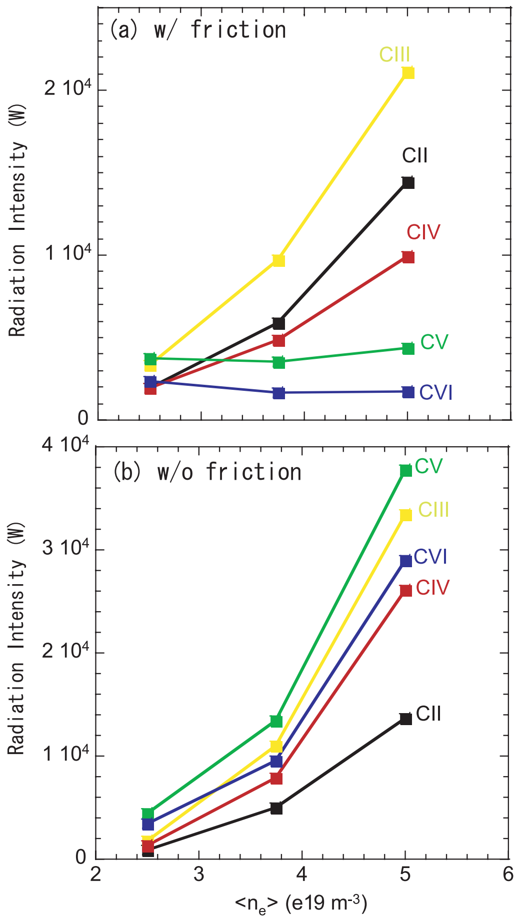

Fig. 6 (a) Radiation intensity integrated in the computational domain for different charge states as a function of density. (b) Same as (a) but with $V_{\mathrm{i}\parallel} = 0$ in impurity transport. black : CII, yellow : CIII, red : CIV, green : CV, blue : CVI.

using vacuum ultraviolet (VUV) monochromators and an extreme ultraviolet (EUV) spectrometer [15], which are installed at the horizontally elongated toroidal section and are tacing the plasma horizontally from the outboard side on the mid-plane. The view angle covers the full vertical range of the plasma at the toroidal section. It is found that the CII radiation is negligibly small in the experiments, whereas it has substantial intensity in the modeling. This is probably because in the modeling, the divertor legs are neglected, which then allows the C^{+1} to reach the ergodic layer. However, in the experiments, they are ionized much earlier downstream in the legs (very near divertor plates) and thus difficult to detect by the limited view angle of monochromators. The obtained line integrated intensity for different charge stages are plotted in Fig. 7 as a function of density. In this plot, the sum of CIII (977 Å) & CIV (1548 Å) and CV (40.27 Å) & CVI (33.73 Å) are plotted rather than each. The radiation of individual charge states shows similar behavior as Fig. 7. By assuming that the intensity is not strong function of toroidal angle, the radiation intensity can be compared between experiments and modeling qualitatively.

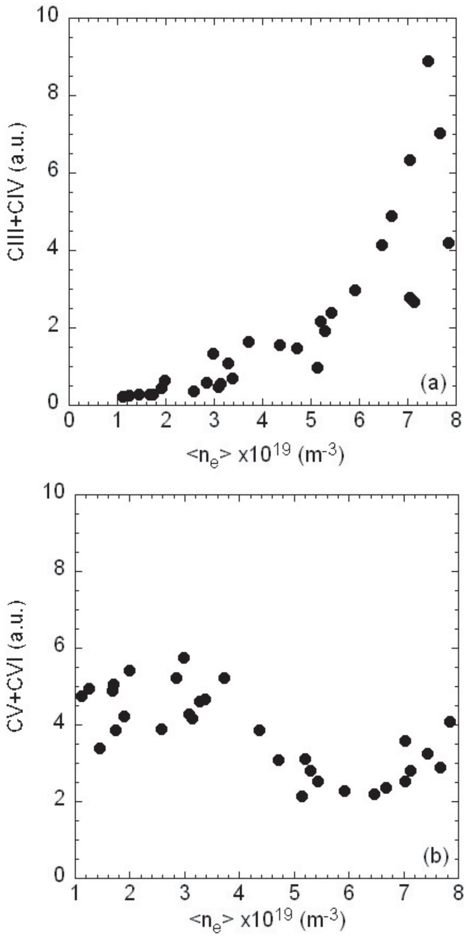

Fig. 7 Radiation intensity from different charge states as a function of density, measured by the VUV monochromators and EUV spectrometer. (a) CIII (977 Å) + CIV (1548 Å), (b) CV (40.27 Å) + CVI (33.73 Å).

The CIII + CIV increases monotonically by an order of magnitude with increasing density; on the other hand, the CV + CVI stays almost constant within a change of factor of two against density scan. In the modeling, we have confirmed that the tendency of Fig. 6 is independent of the selection of view angle These results are in qualitative agreement with the modeling with friction force, Fig. 6 (a), and can be interpreted as a clear experimental evidence of impurity retention in the ergodic layer.

It should be noted that the effective impurity retention is also due to the geometrical advantage of the ergodic layer in the LHD, where the edge surface layer surrounds the plasma in all poloidal and toroidal direction, and thus it can protect the plasma from the impurity neutrals coming from all direction, e.g. impurity released at the divertor plate by plasma flux or at the first wall by charge exchanged neutrals.

5. Implications for High-*Z* Impurity

From Eq. (8), one sees that the balance between the first and second terms on the right-hand side is independent

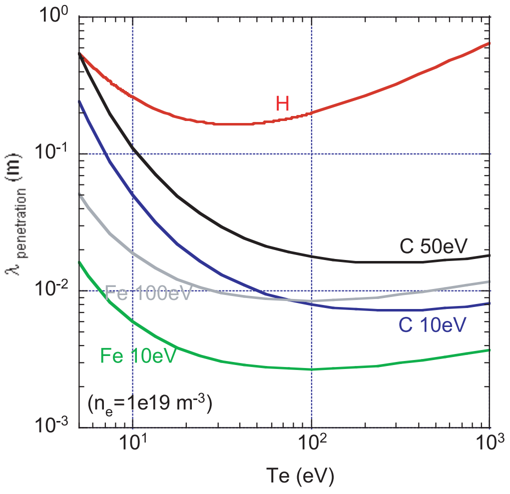

Fig. 8 Estimated neutral penetration length for hydrogen, carbon and iron, indicated with H, C and Fe, respectively.

of the charge Z, because $\tau_s \propto 1/Z^2$, which then cancels with the Z^2 in the numerator.

For the friction force to drive the impurity downstream, the ionization location of impurity species in the present case C^0, should be far downstream of that of the bulk plasma. The larger the separation between the source locations of the impurity and bulk plasma is, the stronger is the retention effect. Because carbon has a lower ionization potential than hydrogen, this is usually the case unless the carbon is injected with very high energy. Figure 8 shows the estimated penetration length of neutral hydrogen, carbon, and iron as a function of electron temperature. Due to the very low ionization potential of Fe^0, 7.9 eV, the penetration length of Fe is even shallower than carbon, indicating that the impurity retention model presented in Section 3 could also apply.

Figure 9 shows the time trace of line radiation intensity of FeXX (132.85 Å) + FeXXIII (132.87 Å) measured by VUV spectrometer, for different plasma density, being normalized with n_e at the center of plasma. From $t = 1.0$ to 2.0 s, the plasma density and temperature was kept constant for each shot. The input power was set as ~8 MW. As the density increases, the normalized intensity decreases gradually, while the intensity at $n_{\text{LCFS}} = 3 \times 10^{19}$ m^{-3} shows a strong increase in spite of the constant plasma parameters during flat top. The increase seems to continue further after $t = 2$ s, although the discharge was terminated just after 2 s. This increase indicates impurity accumulation at the core region. The similar behavior was observed in the low power discharge with ~1 MW [16]. Nevertheless, at the higher density of $n_{\text{LCFS}} = 4 \times 10^{19}$ m^{-3}, the intensity is significantly suppressed and no such accumulation is observed. Compared with the low-density case, the reduction is a factor of 5. With the increase of the density, the electron temperature at the center of the plasma decreases from 2 to 1 keV, i.e., by a factor of 2, due to the fixed input power. However, considering the temperature dependence of the line intensity of FeXX (132.85 Å) + FeXXIII (132.87 Å), which is almost saturated around 1 to 2 keV, the reduction in the measured radiation (normalized by density) indicates reduction in Fe^{+19} and Fe^{+22} at the center of the plasma. Although for analyzing consistently the transport of the high-charge states of iron we need to address the core impurity transport, the behavior is consistent with the prediction of the edge model in the Section 3.

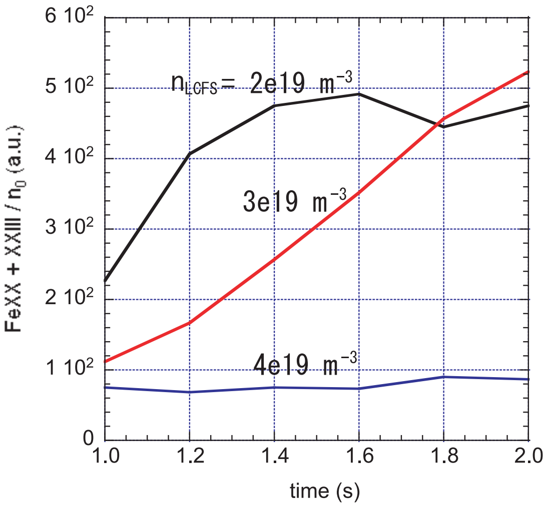

Fig. 9 Time traces of line intensity of FeXX (132.85 Å) + FeXXIII (132.87 Å) measured by VUV spectrometer for different density, at flat top discharge during $t = 1$ to 2 sec. The intensity is normalized with electron density at the center of plasma.

6. Summary

The impurity transport properties in the ergodic layer of the LHD have been analyzed using the edge transport code (EMC3-EIRENE), in comparison with experimental data. The 1D impurity transport model along the field lines predicts impurity retention (screening) when the plasma becomes dense and cold with substantial flow acceleration. This is demonstrated in the ergodic layer of the LHD by 3D numerical simulations. It is found that the edge surface layer plays an important role in the retention, where the ratio of the friction force to the thermal force (Eq. (9)) significantly increases due to the flow acceleration and a decrease in the temperature. The carbon line radiation measurements is compared with the simulation results, where the good qualitative agreement is obtained with the modeling results with friction force, indicating impurity retention in the experiments. It should be noted that the retention effect is also due to the geometrical advantage of the magnetic field structure of the ergodic layer in the LHD, where the edge surface layer surrounds the plasma in all poloidal and toroidal directions. This structure efficiently stops the impurity originating from any locations, i.e., the divertor or the first wall.

Applicability of the model for the high-Z impurity was discussed with respect to the charge dependence and the neutral impurity penetration distance. The brief estimation implies that the mechanism could also apply for the high-Z impurity. The behavior of the measured line intensity of FeXX + FeXXIII against the density change is consistent with the prediction of edge modeling. It is, however, necessary to address the core impurity transport properties for understanding the behavior of high-Z impurity, for which future studies are required.

Acknowledgments

The authors are grateful for the support for the computational resource, AMD Opteron-InfiniBand Cluster Machine, by Grant-in-Aid for Science Research on Priority Areas (Area 465, No.18070005) from the Ministry of Education, Culture, Sports, Science and Technology, Japan. A part of the computational work is also financially supported by the budget code NIFS07ULPP538. One of the authors, M.K., is grateful to N. Yamamoto for the fruitful discussion and the calculation for temperature dependence of the line intensity of Fe.

[1] ITER Physics Basis Editors, Chapter 4, "*Power and particle control*," Nucl. Fusion **47**, S203 (2007).
[2] P.C. Stangeby and J.D. Elder, Nucl. Fusion **35**, 1391 (1995).
[3] C. Breton *et al.*, Nucl. Fusion **31**, 1774 (1991).
[4] M.Z. Tokar *et al.*, Plasma Phys. Control. Fusion **39**, 569 (1997).
[5] M.Z. Tokar, Phys. Plasmas **6**, 2808 (1999).
[6] D.Kh. Morozov and J.J.E. Herrera, Phys. Plasmas **2**, 1540 (1995).
[7] H. Yamada *et al.*, Plasma Phys. Control. Fusion **49**, B487 (2007).
[8] N. Ohyabu *et al.*, Nucl. Fusion **34**, 387 (1994).
[9] Y. Feng *et al.*, Contrib. Plasma Phys. **44**, 57 (2004).
[10] D. Reiter *et al.*, Fusion Sci. Technol. **47**, 172 (2005).
[11] P.C. Stangeby, *The plasma boundary of magnetic fusion devices*, (Institute of Plasma Publishing, 2000) chap.6.
[12] Y. Feng *et al.*, Nucl. Fusion **46**, 807 (2006).
[13] Yu. L. Igitkhanov, Contrib. Plasma Phys. **28**, 477 (1988).
[14] S. I. Krashenninikov *et al.*, Nucl. Fusion **31**, 1455 (1991).
[15] M.B. Chowdhuri, S. Morita and M. Goto, Appl. Optics **47**, 135 (2008).
[16] Y. Nakamura *et al.*, Nucl. Fusion **43**, 219 (2003).